Macromolecules

ARTICLE

pubs.acs.org/Macromolecules

Reinforcement and Polymer Mobility in Silica−Latex Nanocomposites with Controlled Aggregation

Mouna Tatou,[†,‡,∥] Anne-Caroline Genix,[*,†,‡] Ainara Imaz,[§] Jacqueline Forcada,[§] Amélie Banc,[†,‡] Ralf Schweins,[∥] Isabelle Grillo,[∥] and Julian Oberdisse[†,‡,⊥]

[†]Laboratoire Charles Coulomb UMR 5221, Université Montpellier 2, F-34095 Montpellier, France

[‡]Laboratoire Charles Coulomb UMR 5221, CNRS, F-34095 Montpellier, France

[§]Grupo de Ingeniería Química, Facultad de Ciencias Químicas, The University of the Basque Country, 20080 San Sebastian, Spain

[∥]Institut Laue-Langevin, F-38042 Grenoble, France

[⊥]Laboratoire Léon Brillouin, UMR 12 CEA/CNRS, CEA Saclay, F-91191 Gif sur Yvette, France

Supporting Information

ABSTRACT: The tunable structure of silica−latex nanocomposites made of silica nanoparticles (radius ≈ 80 Å) and a copolymer of methyl methacrylate and butyl acrylate−latex beads (radius ≈ 210 Å) has been studied by small-angle neutron scattering and transmission electron microscopy. An aggregation diagram as a function of the control parameters—silica volume fraction and precursor solution pH—has been established. In this aggregation diagram, isoaggregation lines have been identified. It was used to express the small-strain reinforcement factor measured with stress−strain isotherms as a function of volume fraction at fixed aggregation number in the range from 50 to 100. The large-strain properties have been rationalized using the energy needed to rupture samples, and this quantity has been found to present an optimum at intermediate volume fractions (15%). In order to understand the striking rheology of the system, a neutron contrast-matching study has been undertaken by adding deuterated polymer beads. The bead demixing kinetics during annealing has been used to characterize the dynamics in various environments defined by the hard silica structure. In particular, in nanocomposite samples containing 15 vol % of silica the dynamics is found to be blocked.

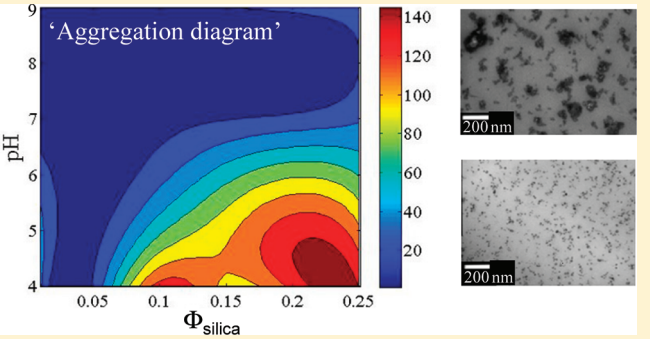

I. INTRODUCTION

Soft−hard nanocomposites made of nanoparticles incorporated in a soft polymeric matrix have been studied both for their fundamental interest, e.g. to discover by which mechanisms the properties of nanocomposites emerge from those of their constituents,[1−5] and for their industrial relevance, e.g. for the car tire industry or the packaging industry seeking barrier properties or fire resistance. The dispersion of often hydrophilic nanoparticles in usually hydrophobic matrices can be achieved in various ways. Individual dispersions may be obtained by hydrophobizing the particles prior to incorporation,[6−11] usually by grafting small hydrophobic molecules as covering agents. Particles may then be entrapped in a polymer matrix e.g. by polymerizing the continuous phase with suspended particles.[11] Alternatively, particles can also be synthesized in situ.[12] Solvent-free methods based on strong shear in extruders or similar devices are typically used in industry,[13] whereas suspensions of both particles and polymer in common good solvents followed by drying[14−18] or coprecipitation[19] are based on specific physicochemical properties of the systems. A drawback of most of the methods outlined above is that they lack a degree of freedom capable of tuning freely the resulting hard phase structure in the polymer matrix.

The silica−latex system based on drying of aqueous colloidal suspensions[20−26] possesses such a degree of freedom because the final nanocomposite structure is reminiscent of the colloidal interactions between silica and latex nanoparticles in the precursor solution before film formation by solvent evaporation. Indeed, the electrostatic interactions between nanoparticles in solution, which depend on pH and ionic strength, determine the final silica structure, for a given drying speed. The silica structure in such nanocomposites has been studied before by scattering techniques,[24,27−32] and it was shown that average aggregate masses ranging from a few nanoparticles to several hundreds could be generated, depending mainly on a simple parameter, the precursor solution pH.[33] Moreover, detailed simulations have been developed to extract the average aggregate structure from the scattered intensities.[34] The structure of pure

Received: June 7, 2011
Revised: August 26, 2011
Published: October 28, 2011

latex films has attracted considerable attention in the past.[21,23,35−38] These scattering studies have been devoted to the structural evolution of the cellular latex under annealing, giving detailed knowledge on the different stages of bead concentration, deformation, and polymer interdiffusion during film formation.

Here, we are interested in mechanical properties, or more exactly rheological ones, as our samples are not cross-linked and thus flow. The rheology of silica−latex nanocomposites has been shown to depend strongly on the physical chemistry of the system. The reinforcement of the rheological properties of the pure polymer by the nanoparticles is usually thought to be due to two effects:[3] a *structural contribution* of the nanoparticles, which includes hydrodynamic reinforcement due to the perturbation of the stress field in the matrix around nanoparticles,[39,40] hydrodynamic reinforcement by aggregates containing both particles and polymer, and finally large-scale interactions, either between particles or between aggregates, leading to a hard percolating network.[41] The structure is thus of primary importance for the rheological properties of the nanocomposites. The second *surface contribution* is due to interactions at the polymer−nanoparticle interface. It depends on a possible surface coverage of the particles, on the degree of covalent or ionic linking between the two phases and on the proximity to the glass-transition temperature, which may favor the formation of a glassy polymer layer (about 1 nm) at the interface.[42,43] Such layers introduce dynamical heterogeneities with a strong impact on the rheology. In the context of reinforcement, an important advantage of the silica−latex system is that the silica structure can be tuned over a wide range while the polymer−nanoparticle interface stays similar for different structures due to absence of covalent bonds.

Measurement of polymer dynamics in nanocomposites has been achieved by several methods, among which one finds fluorescence resonance energy transfer,[44] quasielastic neutron scattering,[45−47] and NMR techniques.[43,48−52] Among the latter, recent low-field NMR experiments using magic-sandwich echo evidenced the existence of at least three kinds of polymer mobilities in filled elastomers.[43] One of them is the immobilized (glassy) layer, which affects the mechanical properties.[53] It should be noted that some controversy exists on the existence and characteristics of such glassy layers. On larger scales, comparable to the radius of gyration (R_g) of the polymer chains, small-angle neutron scattering (SANS) has been shown to be an efficient method,[54−57] with deuterated molecules as a probe. In this paper, a similar method is applied to silica−latex nanocomposites, based on the phase-separation kinetics of incompatible hydrogenated and deuterated polymer latex beads during annealing.

The outline of this article is the following: in section III, the silica structure of new nanocomposite samples ranging up to 25 vol % of silica is studied by SANS and transmission electron microscopy (TEM), and a novel "aggregation diagram" has been constructed. This diagram is then coupled to the rheological data measured in section IV in order to obtain reinforcement as a function of volume fraction of aggregates of a given average aggregation number, which has to our knowledge never been reported before. The incorporation of labeled chains is described in section V, allowing probing of polymer bead mobility as a function of silica content, which sheds light on reinforcement from the point of view of dynamics.

II. MATERIALS AND METHODS

Silica and H-Latex Nanoparticles. Bindzil silica nanoparticles delivered in high pH charge-stabilized aqueous suspensions (30 wt %, pH 9−9.5) were a gift from Akzo Nobel. We have checked by SANS that they were individually dispersed, and their dimensions could be described using a log-normal size distribution (R_{LN} = 78.5 Å and σ = 18%) leading to an average volume of $V_{si} = 2.34 \times 10^6$ Å^3 and a volume-average radius of R_{si} = 82 Å. Contrast variation was employed to determine the scattering length density ($\rho_{si} = 3.64 \times 10^{10}$ cm^{-2}). The hydrodynamic radius determined by DLS was 120 Å.

The hydrogenated polymer latex nanoparticles (H-latex) suspended in water at 30 wt % were a gift from Rhodia. They were charge-stabilized at high pH due to acrylic acid groups added during polymerization. Latex nanoparticle dimensions were characterized by SANS and also obey a log-normal distribution (R_{LN} = 200 Å and σ = 20%), leading to a volume-average radius of 212 Å. Contrast variation gave a scattering length density of $\rho_H = 1.16 \times 10^{10}$ cm^{-2}. The hydrodynamic radius determined by DLS was 240 Å. The particle core was a statistical copolymer of methyl methacrylate (MMA) and butyl acrylate (BuA). The chain mass distribution was determined by SEC calibrated for PMMA in THF (M_w = 133 kg/mol, M_n = 35 kg/mol). ^{1}H NMR in $CDCl_3$ was used to check the chemical composition of the latex particles (45% MMA, 55% BuA). A single glass-transition temperature was observed by differential scanning calorimetry (DSC) (T_g = 17 °C) in spite of the large difference between the monomer T_gs, in agreement with studies by Fytas et al.[58] This value is close to the weighted average (22 °C) of the inverse T_g of the two monomers involved (−24 and 110 °C,[59] respectively). These measurements prove that the copolymer was indeed statistical. The rather high polydispersity index PI = M_w/M_n of 3.8 is due to the lack of control of the emulsion polymerization of these particles of industrial origin.

Synthesis of Deuterated Lattices. Deuterated polymer nanoparticles (D-latex) were purpose synthesized in San Sebastian using a semicontinuous batch method, with perdeuterated MMA and BuA containing 9 D. The synthesis protocol was adapted from similar protocols.[60] In short, MMA and BuA monomers were distilled under reduced nitrogen pressure. All other materials were used as received. Potassium persulfate ($K_2S_2O_8$, Merck) and sodium dihydrogen phosphate ($NaH_2PO_4 \cdot H_2O$, Merck) were used as initiator and buffer, respectively. The surfactant used for stabilization was sodium dodecyl sulfate (SDS, Merck) (6 wt % with respect to the total monomer mass). Deionized water was used throughout. The semicontinuous emulsion copolymerization was carried out at 80 °C in a 1 L glass reactor fitted with a reflux condenser, stainless steel stirrer, sampling device, nitrogen inlet, and a feed inlet tube. The initial charge in the reactor was the surfactant, buffer, initiator, and water. The feed was divided into two streams. The first was a solution of initiator, surfactant, and buffer in water (feeding rate = 0.26 mL/min), and the second was a mixture of both monomers in the required ratio to maintain monomer-starved conditions (feeding rate = 0.07 mL/min). The monomer and aqueous feeds were calculated to finish the addition in 1 h. Subsequently, the polymerization was continued in batch for 4 h. Total conversions of the perdeuterated comonomers to D(MMA-*co*-BuA) copolymer were achieved.

This protocol lead to latex particles of radius $R_{Guinier} = (5/3)^{1/2} R_g$ = 125 Å measured in the Guinier regime by SANS. The data could be described with a log-normal size distribution (R_{LN} = 94 Å and σ = 25%, volume-average radius $\langle R \rangle_v$ = 103 Å). The experimentally determined scattering length density was $\rho_D = 6.4 \times 10^{10}$ cm^{-2}. The hydrodynamic radius determined by DLS was 135 Å. The T_g found by DSC was 47 °C, which is consistent with the higher MMA proportion determined by ^{1}H NMR in $CDCl_3$: 72% MMA, 28% PBuA. SEC was used to determine the chain mass distribution (M_w = 218 kg/mol, M_n = 87 kg/mol, PI = 2.5).

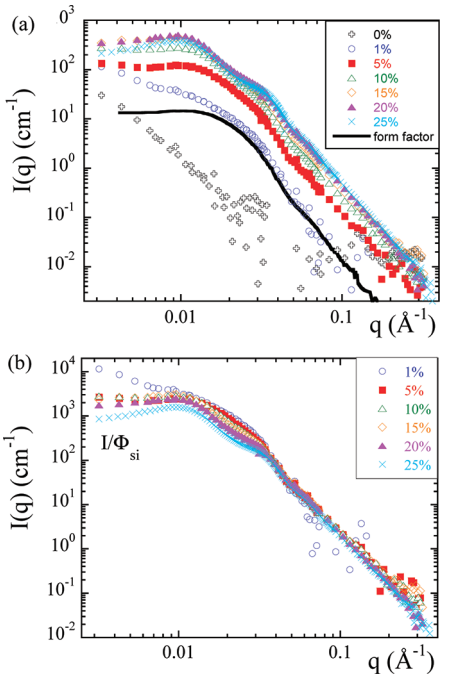

Figure 1. (a) Scattered intensity $I(q)$ of a series of silica−latex nanocomposites formed at pH 7, with varying silica volume fraction (Φ_{si} = 0−25 vol %). (b) Same data in the reduced representation $I(q)/\Phi_{si}$.

The form factor for both lattices and silica particles including contrast variation are shown in the Supporting Information.

Nanocomposite Formulation and Film Formation. Bubble-free millimeter-thick silica−latex films were formed by slow drying in Teflon molds at 65 °C for 3 days, after deionization and degassing of solutions, and immediate pH adjustment to the desired value using NaOH. Samples were cut, and their thickness was brought to about 1 mm using sandpaper for stress−strain isotherms and SANS measurements with H-latex only. D-containing samples for scattering were thinner (0.2−0.3 mm) to avoid multiple scattering.

Stress−Strain Isotherms and Stress Relaxation. Uniaxial deformation of samples of approximate dimensions 30 × 10 × 1 mm^3 was imposed using a homemade strain rig working in a silicon oil bath (T = 65 °C) for temperature control, and the force was recorded with an HBM force sensor (20 and 100 N). In order to determine the real stress σ in the sample, sample volume conservation and affine deformation were used to estimate the sample cross section, which is a good approximation up to intermediate elongation ratios λ, where λ is given by L/L_0, where L is the length of the sample and L_0 the initial length. λ was chosen to increase exponentially with time, with a constant gradient of $\dot{\gamma} = 10^{-3}$ s^{-1}. All samples show some viscous flow at short time scales; such low $\dot{\gamma}$ probe the viscoelastic contributions on longer time scales. Samples were deformed up to rupture, and energy up to rupture per unit sample volume was obtained by integrating over the force. This energy depends on the kinetics of fracture formation, which in turn depends on the gradient. This is why the gradient has been kept fixed to allow comparison. Young's modulus E has been deduced from the low deformation slope of the stress−strain isotherms, $E = d\sigma/d\lambda|_{\lambda=1}$. The reinforcement factor, E/E_{matrix}, was obtained by normalizing to the modulus of the silica-free (but otherwise identical) latex matrix. Error bars on Young's modulus and rupture energy have been evaluated by comparison of a set of identical samples and amount to 10% for both quantities. Stress relaxation curves of selected samples were measured by stretching rapidly ($\dot{\gamma}$ = 0.5 s^{-1}) and stopping the elongation before rupture. Stress was monitored as a function of time for 1 h.

Nanocomposite Structure Determination. Transmission electron microscopy was performed on thin slabs of dilute sample ($\Phi_{si} \leq 5\%$, thickness 70 nm) on a Jeol 1200 Ex II microscope. Small-angle neutron scattering was performed on beamlines D22 at Institut Laue-Langevin (ILL) (three configurations, defined by sample-to-detector distance D and incident neutron wavelength: D = 17 m; D = 5 m; D = 1 m, all at 6 Å) and PACE at Laboratoire Léon Brillouin (LLB) (D = 4.5 m, 12 Å; D = 4.5 m, 6 Å; D = 1 m, 6 Å). Empty cell or empty beam subtraction, calibration by 1 mm light water in Hellma cuvettes, and absolute determination of scattering cross sections $I(q) = d\Sigma/d\Omega$ per unit sample volume in cm^{-1} were performed using standard procedures,[61] namely an incoming beam measurement at LLB and ILL. Incoherent background was estimated from the known high-q Porod law of silica particles or interfaces between H and D zones.

Dynamic Light Scattering (DLS). Experiments were performed using a standard setup by Brookhaven Instruments Co. (BI-900AT). All measurements were performed at a scattering angle θ = 90°, using a 100 mW argon ion laser with in-vacuo wavelength λ = 514 nm. The sample was thermostated at T = 24.6 ± 0.1 °C.

III. SILICA STRUCTURE IN NANOCOMPOSITES

The dispersion of the nanoparticles in silica−latex systems depends crucially on the interaction potential between particles in solution, which in turn evolves with concentrations of particles and ions during the drying process. In this paper, the silica structure in the nanocomposites is measured by SANS and TEM as a function of silica volume fraction Φ_{si} and the precursor solution pH (between 4 and 9).

In Figure 1a, a series of scattered intensities for samples made from precursor solutions at pH 7, with Φ_{si} ranging from 0 to 25%, are shown. The pure polymer film is seen to display some structural heterogeneity, the scattering of which remains orders of magnitude below the intensity due to the silica nanoparticles. This film is seen to be nicely homogeneous and void-free on this scale of observation, as can be seen in a TEM cliché of the silica-free sample (Supporting Information). In presence of silica, the intensity decays with $1/q^4$ in the Porod regime, as expected for silica particles in polymer. Indeed, the rescaled form factor of colloidal silica beads measured independently in solution can be nicely superimposed in the high-q range in Figure 1a. We have also checked that the normalized intensities I/Φ_{si} superimpose at $q > 0.03$ Å^{-1} (cf. Figure 1b). At intermediate angles, some weak oscillations reminiscent of the form factor oscillations of the silica nanoparticles are found. At low q, finally, an interaction peak is observed. It becomes stronger as the silica volume fraction increases, and it corresponds to a dominant distance in the silica nanoparticle dispersion. This peak is the signature of the distance between silica aggregates, and it is possible to describe the interaction by an aggregate−aggregate structure factor, whereas the aggregates themselves can be modeled by assemblies of particles.[34,62−65] Such complete modeling proves that the simple picture of interacting average aggregates is compatible with the measured intensity and that the aggregation number N_{agg} of these average aggregates can be estimated using a simple cubic model:

$$N_{agg} = \left(\frac{2\pi}{q_0}\right)^3 \frac{\Phi_{si}}{V_{si}} \quad (1)$$

where q_0 is the peak position and V_{si} the average volume of one silica bead. Curves very similar to those displayed in Figure 1 have

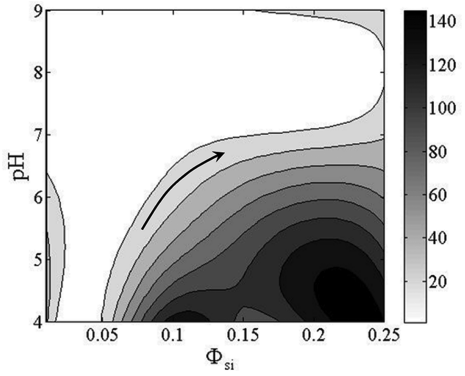

Figure 2. "Aggregation diagram" of average aggregation number N_{agg} as a function of silica volume fraction and precursor solution pH. The arrow indicates a possible series of samples at constant N_{agg}.

been measured for the same series in silica volume fraction, but for different pH values (4, 5, and 9), and they are displayed in the Supporting Information. The aggregation numbers extracted from all the data following eq 1 have been summarized under the form of an "aggregation diagram" in Figure 2.

In some cases at low concentrations, there is no peak in the intensity, and namely for the 1% samples, only lower bounds can be estimated from the low-q upturns. In presence of a well-defined low-q plateau, estimates for N_{agg} and its evolution with Φ_{si} and pH were obtained from I_0 by fitting a Guinier law to the curvature at small angles:

$$I = I_0 \exp\left(-\frac{q^2 R_g{}^2}{3}\right) \tag{2}$$

I_0 can then be related to the average aggregation number N_{agg}:

$$I_0 = \Delta\rho^2 \Phi_{si} V_{agg} \tag{3a}$$

$$N_{agg} = \frac{V_{agg}}{V_{si}} \tag{3b}$$

where $\Delta\rho$ is the scattering contrast between silica and the polymer and V_{agg} the volume of silica in each aggregate. In eqs 3, it is supposed that all aggregates have the same average mass and that they do not interact, which implies that it can only be used at low Φ_{si}. Note that Figure 2 is based on a numerical interpolation of results of eqs 1−3. The general tendency is obvious: in Figure 2, the average aggregation number is found to increase predominantly with volume fraction Φ_{si}, whatever the pH. It is typically in the range from a few units to more than one hundred. If one reads Figure 2 as a function of pH, a higher precursor solution pH yields better silica nanoparticle dispersions. There seems to be a critical pH value, around 6, below which a strong increase in aggregation number is observed (cf. a vertical cut at higher concentrations in the Supporting Information).

Finally, a deeper analysis of the scattering data can be made by combining the radius of gyration (eq 2) and the aggregation number (eq 3). The radius of aggregates R_{agg} of fractals can be extracted from R_g

$$R_{agg} = R_g \sqrt{\frac{d+2}{d}} \tag{4}$$

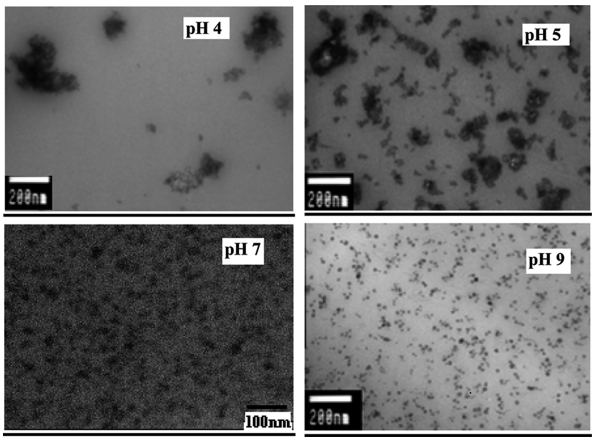

Figure 3. TEM micrographs of nanocomposites with 1 vol % of silica nanoparticles, formed at different solution precursor pH as indicated on the graphs. Scale bars: 100 or 200 nm. Higher concentration (5%) is shown in the Supporting Information.

and can be related to the aggregate mass by a power law with a fractal dimension d:[66]

$$N_{agg} = \left(\frac{R_{agg}}{R_{si}}\right)^d \tag{5}$$

For large aggregates (e.g., pH 4, 1% of silica: R_{agg} = 550 Å, N_{agg} = 44), the fractal dimension is 2.0 ± 0.1. This is also compatible with the scattering at intermediate q in Figure 1. Alternatively, a compacity of aggregates κ can be defined as

$$\kappa = N_{agg}\left(\frac{R_{si}}{R_{agg}}\right)^3 \tag{6}$$

The resulting compacity is 14.5%. For smaller aggregates produced at higher pH, the aggregation number decreases, which leads naturally to a compacity increase, as well as a higher nominal fractal dimension, but such aggregates are too small for this concept to apply.

A series of corresponding transmission electron microscopy clichés taken at various pH values and at a low volume fraction (1%) to reduce aggregate overlap are shown in Figure 3. One observes different states of aggregation, better dispersion being obtained for higher pH values. It has to be noted, however, that the TEM pictures may contain artifacts. First of all, only a small region of the sample is observed, whereas scattering stems from a macroscopic region of the size of the neutron beam. Second, the TEM clichés present a 2D projection of the real structure, which may cause erroneous interpretations due to particle overlap. In spite of these limitations, it seems obvious that the electron microscopy results are in good qualitative agreement with the scattering results: nanoparticle aggregation in nanocomposites is strongly increased at low pH.

To summarize the dependence of average aggregation on precursor solution pH and Φ_{si}, it is confirmed that N_{agg} depends on both parameters. Increasing the silica volume fraction along a line of fixed pH in Figure 2, the aggregates become more massive and simultaneously their number density goes up. This leads to two conclusions: (i) The dependence of the average aggregation number on pH provides us with a convenient way to tune the structure of the hard silica phase through the physical chemistry.

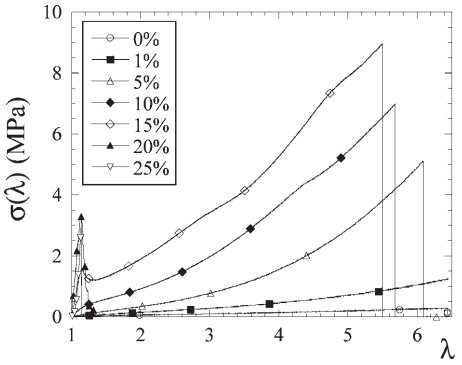

Figure 4. Stress−strain isotherms at T = 65 °C for samples of varying silica volume fractions Φ_{si} ranging from 0 to 25%, formed with precursor solutions at pH 7.

(ii) A new opportunity arises if we wish to characterize the impact (e.g., on rheology and polymer dynamics) of the number density of aggregates at a fixed average aggregation number. Indeed, by changing both pH and Φ_{si} simultaneously, one can move along an isoaggregation line in Figure 2 as exemplified by the arrow. To our knowledge, our experimental system is among the very rare systems where this is possible, owing to the existence of a second control parameter—solution pH—apart from the filler volume fraction.

IV. STRESS−STRAIN ISOTHERMS OF NANOCOMPOSITES

In this section, the strikingly variable rheological properties of silica−latex nanocomposites will be discussed. As already noted, these properties are controlled by both a structural and an interfacial contribution. The interfacial one stays roughly constant in our system (at fixed T and fixed surface chemistry). In some systems, the presence of glassy layers, with possible bridging between particles, has been evidenced.[43,51] Their primary effect is to increase the hard particle diameter, which pushes reinforcement to higher values. In section V, the presence of glassy layers will be discussed as a possible explanation for the kinetics of probe molecules. Here, the impact of the second contribution—the microstructure—on reinforcement will be investigated. Stress−strain isotherms of our nanocomposite samples have been measured in the viscoelastic domain, at 65 °C, above the glass-transition temperature. By combining the previously determined nanoparticle dispersion with the rheological results, a first step toward the reinforcement contribution of aggregates of controlled aggregation number is presented.

In Figure 4, the stress−strain isotherms for the same nanocomposite series as in Figure 1 (pH 7, with silica content varying from 0 to 25 vol %) are displayed (cf. Supporting Information for pH 4, 5, and 9, with Φ_{si} up to 25 vol %). At low silica volume fraction, the stress is seen to increase continuously with deformation, up to rupture observed at rather high deformations of more than 500%. As more silica is added, the stress increases over the entire range of deformation. Samples stay extensible up to ca. 15% of silica loading. Only at the highest Φ_{si}, the samples become brittle and break early (λ = 1.1−1.3).

Young's modulus—in the range from 0.1 to 55 MPa—can be determined, and its reinforcement factor, E/E_{matrix}, has been calculated. E/E_{matrix} highlights the contribution of the silica, as the evolution of the matrix properties with pH is canceled in a first approximation. The reinforcement factor turns out to be a strongly increasing function with silica volume fraction: considerable reinforcement is achieved in this system, reaching values of several hundreds above silica volume fractions of 10%. Examining the dependence on the precursor solution pH, the reinforcement is lower at high pH, but even there very high values are reached. Keeping in mind that the modulus of pure silica (ca. 30 GPa) is about 3×10^4 times higher than the one of a rubbery matrix, such high reinforcement factors suggest the formation of a silica network.

In the past, we have plotted the reinforcement factor of Young's modulus as a function of silica volume fraction at fixed pH.[31] Remembering that at fixed pH aggregates both grow and become more numerous—as illustrated by the aggregation diagram displayed in Figure 2—we now attempt to obtain the reinforcement factor as a function of concentration of aggregates of fixed average mass. This is achieved by plotting E/E_{matrix} in Figure 5a as a function of N_{agg} as taken from Figure 2 for the different volume fraction series.

The result shows quite scattered data illustrated by the zones in the figure, but a clear increase of E/E_{matrix} with silica volume fraction is found. We have chosen several aggregation numbers (N_{agg} = 50, 75, and 100) illustrated by dotted lines in Figure 5a and plotted the average reinforcement *at fixed* N_{agg} as a function of Φ_{si} in Figure 5b. There, the error bars were obtained from the width of the represented zone in Figure 5a.

In Figure 5b, the reinforcement factor at fixed aggregation number is found to follow a neat tendency and a strong increase with silica volume fraction. On the contrary, the aggregation number itself is seen to have little impact on the reinforcement factor within error bars. In Figure 5b, we have undertaken an analysis of the reinforcement factor of Young's modulus, comparing a single curve to the general tendency of all data points, in terms of a simple model.[1,2,67−70] We have compared the Einstein−Smallwood equation with the quadratic term to the data:

$$\frac{E}{E_{matrix}} = 1 + 2.5\Phi_{agg} + 14.1{\Phi_{agg}}^2 \quad (7)$$

Following eq 6, the total volume fraction occupied by the aggregates is related to the nominal silica volume fraction by

$$\Phi_{agg} = \frac{\Phi_{si}}{\kappa} \quad (8)$$

The Einstein−Smallwood result for a compacity of κ = 15%, plotted in Figure 5b, is found to stay well below the observed reinforcement. An unphysical choice (κ = 5%), which implies $\Phi_{agg} > 1$, may be used to fit the data. As already pointed out, the formation of a strong silica network is probable, which can not be described by a dilute aggregate model (eq 7).

The presence of nanofillers in the matrix modifies also the stress at large deformation and the elongation at rupture λ_{rupt}. The limiting cases of the influence of filler on rupture are obvious: elastomeric samples break at very high strains but low stresses, whereas samples at high silica loadings become brittle and break under high stress at a low deformation. The range of filler volume fraction chosen in our experiments allows us to investigate the zone between these two extremes. The concomitant increase in stress and decrease in extensibility suggests that there is an optimum in silica concentration, where the

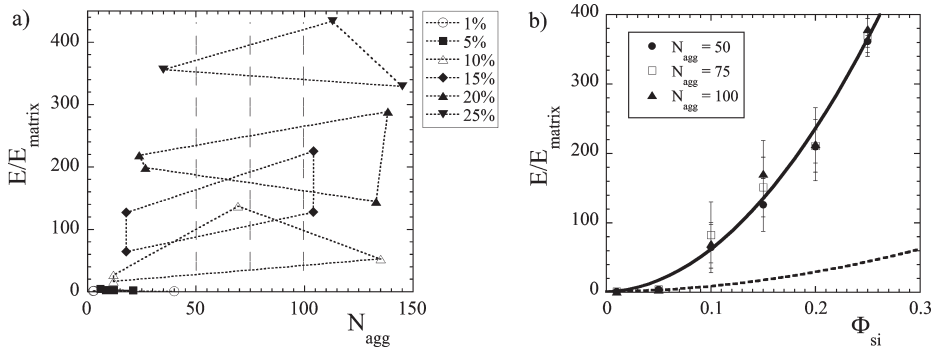

Figure 5. (a) Reinforcement factor of Young's modulus as a function of the average aggregation number for different silica volume fractions (Φ_{si} = 1−25%) and pH values. (b) Same reinforcement as a function of silica volume fraction, for different aggregation numbers. Reinforcement at low volume fractions (1 and 5%) has been estimated by extrapolation from (a). The broken line is the Einstein prediction including the quadratic term with κ = 15%; the solid line is an unphysical fit with κ = 5% (see text).

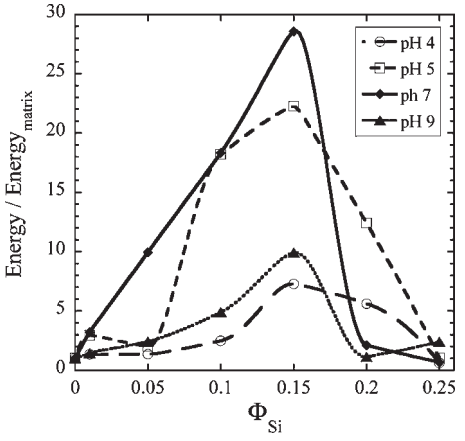

Figure 6. Reinforcement factor of rupture energy Energy/Energy$_{matrix}$ as a function of silica volume fraction Φ_{si} for nanocomposites with different precursor solution pH (from 4 to 9).

reinforcement effect is strongest. A way to analyze this dependence is to determine the mechanical energy needed to reach rupture, per unit volume of sample. The result is expressed as the reinforcement relative to the rupture energy of the silica-free samples, Energy/Energy$_{matrix}$, and plotted in Figure 6 as a function of silica volume fraction for different pH values. A pronounced maximum is found for pH 7, at Φ_{si} = 15%. A shallower maximum is also present for the other pH values, at the same critical volume fraction. Comparing the height of the maxima for different pH, an optimum value is found at pH 7.

We now try to rationalize our finding on the reinforcement in the light of the available structural information. First of all, Young's modulus at fixed aggregation number increases strongly with Φ_{si}, suggesting network formation,[71] but shows little dependence on N_{agg} in the range generated here. Second, the rupture energy shows a strong maximum at 15% whatever the pH and thus also whatever the structure (N_{agg}) in our range. Our interpretation is based on percolation of the silica network, which occurs as a function of Φ_{si}. Once percolated, the system becomes brittle, whereas it reaches high reinforcement (E/E_{matrix}) when approaching percolation, due to energy-dissipating aggregate rearrangements. All experimental systems are seen to percolate at approximately the same volume fraction, around 15%. This seems to be at odds with the different aggregation numbers, as bigger aggregates (assuming a fractal-type structure) are less compact and thus reach percolation earlier. We have therefore estimated the compacity of fractal aggregates as a function of aggregation number, which reads following eqs 5 and 6:

$$\kappa = N_{agg}^{(d-3)/d} \quad (9)$$

κ decreases slowly with N_{agg}, and in the range of aggregation numbers determined by SANS for this system (N_{agg} = 20 to 100 at 15% of silica), the compacity is estimated to stay between 10 and 20%. Note that for low N_{agg} a cutoff which takes the breakdown of the fractal law into account would be needed. To conclude, the silica volume fraction is the principal parameter governing the energy needed to break a sample, as it governs percolation. The role of the pH and thus aggregate structure is secondary and influences not the shape but the prefactor of the rupture energy curve. One must keep in mind, however, that our conclusions based on a restricted range of aggregation numbers cannot be generalized to more aggregated systems.

We have seen that the reinforcement factors reach values of up to several hundred and that this strong reinforcement can be related to the space-filling properties of the nanoparticle aggregates. A point which we have not yet discussed is that the percolation point may be shifted to lower nominal volume fractions due to possible glassy layers, through an increase of the effective filler size and thus volume fraction. For a given filler microstructure, the dynamical properties of the polymer may thus modulate the reinforcement. In the following section, dynamics are now studied through the demixing kinetics of deuterated probes.

V. ZERO-AVERAGE CONTRAST SILICA MATCHING AND POLYMER BEAD DEMIXING KINETICS

In case of compatible polymers, the incorporation of deuterated probe molecules can be done by following the latex route to study both individual chain structure[14,15,72−75] and polymer dynamics.[57] The introduction of deuterated latex beads in the mixed suspension of the industrial Rhodia latex and silica nanoparticles offers several new parameters. We have used purpose-synthesized D-latex beads ($\langle R \rangle_v$ = 103 Å), different amounts of which can be added to the suspension, thus leading to different average scattering length densities of the polymer

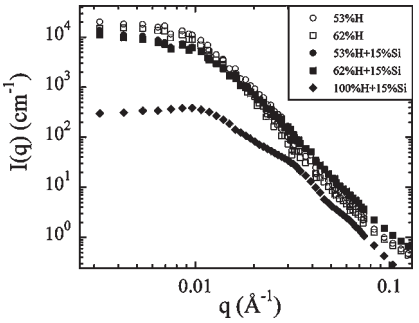

Figure 7. Scattered intensity I as a function of scattering wave vector q from nanocomposite films (pH = 9) with different H/D ratios allowing silica matching: 53% H (circles) and 62% H (squares). Empty symbols are for the pure samples and plain ones for those with 15% silica. Intensity of both filled samples has been corrected for the noncontributing silica by dividing by $(1 - \Phi_{si})$. Data obtained from a fully protonated nanocomposite film with 15% silica (pH = 9) are added for comparison.

matrix ρ_m:

$$\rho_m = \Phi_H \rho_H + \Phi_D \rho_D \tag{10}$$

where Φ_H and Φ_D are the volume fractions of the matrix ($\Phi_H + \Phi_D = 1$). Here, we have set $\rho_m \approx \rho_{Si}$, and we will demonstrate that the silica scattering does not contribute, in agreement with the zero-average contrast condition for silica in our purpose-prepared samples. The use of a different stabilizing method in the D-latex—SDS instead of a mixed surface layer including acrylic acid—makes the two polymer beads immiscible, as will be shown in the rest of this section. Compatible H−D-latex films issued from latex with the same surface layer will be discussed in a forthcoming paper.[76] The demixing kinetics during annealing after film formation—characterized by SANS—can be used as a signature of the polymer bead dynamics. We will show that the latter conveys information on the hindrance induced by the surface interactions and the hard environment formed by the aggregated silica structures.

Reaching zero-average contrast conditions for the silica nanoparticles is less trivial than one might suspect.[73,74] We have started with an independent solvent contrast variation of the silica and H- and D-latex nanoparticles. The scattering length density of our silica—3.6 × 10^{10} cm^{-2}—corresponds to a mixture of Φ_H = 53 vol % and Φ_D = 47 vol % of latex. Two H/D ratios have been explored (cf. ref 77 for a complete analysis of the working range of acceptable ratios), and satisfying silica matching has been found by SANS for both ratios. The results are shown in Figure 7, where $I(q)$ is plotted for 53% H/47% D and 62% H/38% D, without and with 15% of silica at pH 9. The H/D ratio is seen to have virtually no impact on the scattering curves, which is to be expected given the similar value of the product $\Phi_H\Phi_D$. With silica, the low-q intensities are found to be almost a factor of 2 below the pure H/D films, whereas from 0.02 Å^{-1} on, the data are quite close. We have accounted for the presence of silica by dividing the intensity of silica-containing H/D films by a prefactor $(1 - \Phi_{si})$ in Figure 7, and this is insufficient to explain the observed difference with and without silica. For comparison, we have also superimposed the silica scattering measured in hydrogenated films (100% H) at Φ_{si} = 15% and solution pH 9. Under perfect matching conditions (53% H), this signal would vanish, and in the other case (62% H), it would be reduced by a factor of 30. In neither of these cases, the silica would have any appreciable impact on the total intensity curves: already in the worst case of full contrast shown in Figure 7, the signal is far weaker than the observed $I(q)$. Thus, we may conclude that there is no influence of the silica structure found on the scattered intensities for the chosen H/D ratios, proving insensitivity of the system to the exact matching ratio.

If the only measurable contribution to the total intensities in Figure 7 stems from the H and D zones, then the scattering can be described using the formalism developed by Des Cloizeaux.[78−81] For a volume-spanning mixture of identical H and D zones of volume V_z, the scattering is proportional to the average form factor of such zones:

$$I(q) = \Phi_H\Phi_D\Delta\rho^2 V_z P(q) \tag{11}$$

where $P(q)$ is the form factor normalized to 1 at low q. Such an estimation extracted from $I(q \rightarrow 0)$ yields an increase in zone radius ($4\pi/3R^3 = V_z$) from 165 Å to about 200 Å, with and without silica, respectively. The H- and D chains are thus not molecularly dispersed but keep the memory of the original latex beads, as also found in previous studies on cellular latex films.[35,36] The higher average value means that the initially smaller D particles (103 Å) merge to form larger objects during film formation. Apparently, this process is hindered by the silica, yielding a smaller radius (165 Å) in its presence than in its absence (200 Å). In conclusion, the difference with and without silica in Figure 7 can thus not be attributed to the silica signal but very well to the presence of silica influencing the bead merging kinetics.

For a finer description using zones of different sizes, V_z(H) and V_z(D), the data can be weighted accordingly:[79,80]

$$\frac{\Delta\rho^2}{I(q)} = \frac{1}{\Phi_H V_z(H) P_H(q)} + \frac{1}{\Phi_D V_z(D) P_D(q)} \tag{12}$$

Note that in this approach the sample is described geometrically, as an ideal mixture of space-filling zones, the growth of which is reflected in changes over the whole q-range. An alternative approach would be to adapt for beads the random phase approximation (RPA) usually applied to chains,[82,83] with a Flory−Huggins interaction parameter χ, by adding a term $-2\chi/V_0$ to eq 12, where V_0 is the average bead volume. A change in low-q intensity can then be interpreted as the increase of concentration fluctuations controlled by χ. χ does not, however, influence the high-q behavior: concentration fluctuations of beads of constant size always give rise to the same Porod scattering.

A direct evaluation of the average zone size from the scattered intensity using eq 11 in the Guinier and Porod regime is possible: the low-q intensity describes the average volume of the zones, R_g reflects their spatial extension, and the specific surface is given by the Porod constant. As we will see in the next paragraphs, these three numbers are rather close, which hints in favor of a geometric description in terms of a growth of the volume of the zones, and this is what will be used here. However, a combination of both effects, bead−bead interaction and growth, cannot be excluded. In the Supporting Information, it is shown that comparable results are obtained with such a model, if the ratio of the H- and D-bead radii is kept fixed in order to compensate for the introduction of an additional fit parameter χ. In particular, in absence of silica where strong changes are observed, χ vanishes with increasing T, thereby a posteriori justifying the geometric approach (eq 12).

Table 1. Annealing Histories Applied to Samples of Identical Origin

code	annealing process
0	before the film formation (in latex)
A	directly after film formation, 3 days, 65 °C
B	100 °C, 2 weeks
C	110 °C, 1 week
D	120 °C, 1 week
E	D + 125 °C, 3 weeks

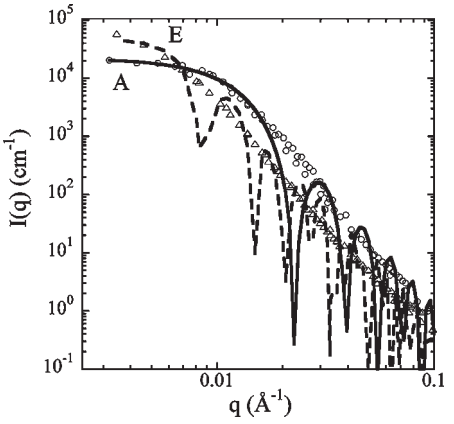

Figure 8. Scattered intensity for two samples obtained after two annealing histories A (circles) and E (triangles) (see Table 1 for details) for 0% silica and 53% H. Lines are fits using eq 12.

In order to follow the polymer demixing as a function of silica content, we have annealed nanocomposite samples during up to 4 weeks, at temperatures between 100 and 125 °C. The annealing histories are summarized in Table 1. They were designed to test the influence of both annealing time and temperature. Annealing processes were applied to different samples cut from four H/D nanocomposites at 0% and 15% silica and 53% H and 62% H, respectively. This allows comparison of samples of identical origin. Note that we have checked that the silica structure at 15% does not evolve with annealing.[77]

As outlined above, the information contained in the scattered intensity from the H and D zones shown in Figure 8 can be summarized with three numbers: for annealing history A, e.g., the equivalent sphere radii are $R(I\rightarrow 0)$ = 200 Å, $R_{Guinier}$ = 210 Å, R_{Porod} = 205 Å. From the intensity increase (from A to E in Figure 8), it is obvious that all three key features evolve toward larger zones: for case E, the radii are $R(I\rightarrow 0)$ = 315 Å, $R_{Guinier}$ = 430 Å, R_{Porod} = 430 Å. We thus know that the zones are globular, space-filling objects. The easiest model reproducing these three values is the form factor of spheres; however, the single-zone model (eq 11) with spheres is compatible with these three features only for the silica-free case A. The model accounting for H and D zones of different volume can be applied following eq 12, with the form factor of a sphere in both cases. With two fitting parameters, R_H and R_D, the radii of the H and D zones, we obtain a nice description of all our data (e.g., case E in Figure 8). It should be mentioned that (i) bidisperse distributions of spheres are not space-filling, but are only used to reproduce the key values, and (ii) it would be straightforward but without further benefit to adjust with a sphere model with an effective polydispersity.

The equivalent sphere radii for these zones have been plotted in Figure 9 as a function of the annealing process. In samples without silica, H- and D-zone radii are found to increase strongly: H zones grow by a factor of 2.6 and D by a factor of 2.2. During annealing, the ratio between H and D radii thus stays scattered around its initial value of two, indicating similar growth. In presence of 15% silica, the zones appear to be blocked around 280 Å (H) and 170 Å (D). Compared to the initial bead sizes, the increase of each zone is thus smaller and comparable (1.7 for H, 1.3 for D). In conclusion, the size of zones grows considerably only in absence of silica during annealing.

A striking feature of Figure 9 is the acceleration of the structural reorganization between annealing history A and B (i.e., from 65 to 100 °C). Segmental dynamics of such a system has been studied by Fytas et al. using dielectric spectroscopy.[58] It was found that the relaxation time decreased by almost 4 orders of magnitude from 65 to 100 °C and by less than a decade from 100 to 120 °C. This indicates the evolution of molecular mobility with the same tendency as our findings.

We have sought an independent method providing evidence of the demixing process. DSC can be used to detect the glass-transition temperature of the polymer blend. In molecularly mixed polymer blends, only a single broad calorimetric T_g is usually detected.[84] H and D lattices having different glass transitions; the DSC thermograms (shown in Supporting Information) prove the existence of two distinct domains, the T_g of which is close to the ones of the pure compounds, 17 and 53 °C, respectively.

The evolution of the radii of the H and D zones gives access to their local mobility,[57] which seems to be forced by the incompatibility between the polymer beads with different stabilizing layers. Demixing may involve global bead motion, but probably also chain diffusion triggered by interactions and concentration differences. In the presence of silica, demixing may be hindered by different mechanisms, including jamming or bottleneck effects,[85] sticky interactions between silica and latex beads, or glassy polymer zones of reduced dynamics. All these mechanisms may affect interparticle interactions and reinforcement.

Here, we have constructed a simple ad-hoc model rationalizing the initial domain growth as the coalescence of H (or D) latex beads of initial volume, V_0. The H beads are initially distributed randomly in space, and a number of them, $N = V_f/V_0$, are needed to form the coalesced zone of volume V_f as observed after an annealing time Δt. This process defines a typical length scale L_c over which the beads need to travel, in a time Δt, and the diffusion coefficient D can thus be determined and related to the local viscosity η via the Stokes−Einstein equation:

$$D = \frac{L_c^2}{\Delta t} = \frac{kT}{\mu} = \frac{kT}{6\pi\eta R_0} \tag{13}$$

where R_0 is the initial radius of the latex beads, μ the mobility, k the Boltzmann constant, and T the annealing temperature. The typical length scale L_c can be estimated assuming a locally cubic spatial distribution, which gives for instance, in the case B (Table 1) for N = 8:

$$L_c = \frac{\sqrt{3}}{2}\sqrt[3]{\frac{V_0}{\varphi_H}} \tag{14}$$

dx.doi.org/10.1021/ma2012893 |*Macromolecules* 2011, 44, 9029–9039

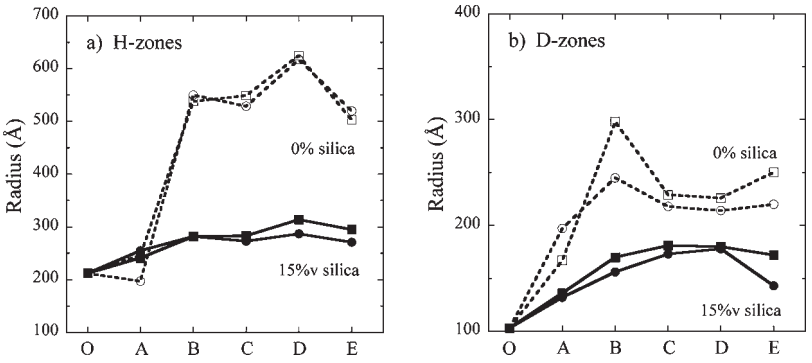

Figure 9. Sphere radii for the H (a) and D zones (b) as a function of the annealing histories for two different H/D ratios in the nanocomposites: 53% H (circles) and 62% H (squares). Empty symbols are for the pure samples, and full ones for those with 15% silica. See Table 1 for annealing details.

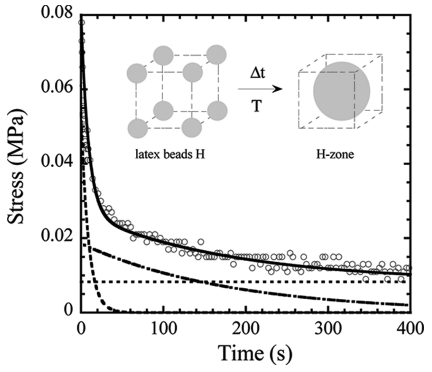

Figure 10. Stress relaxation as a function of time after a rapid elongation ($\dot{\gamma}$ = 0.5 s^{-1}, λ = 1.35) for a fully hydrogenated silica-free latex film at pH 9 and 100 °C. Full line is a fit of a constant level (dotted line) plus two single exponentials with a characteristic time τ_1 = 9 s (dashed line) and τ_2 = 180 s (dash-dotted line). In the inset, a sketch of the coalescence model for N = 8 is shown.

This model leads to an estimated local viscosity in absence of silica of $\eta = 12 \times 10^6$ Pa s (respectively 18×10^6 Pa s for case C). Note that a similar calculation for coalescence of D beads gives an equivalent result for the viscosity (24×10^6 Pa s). Note that a shortcoming of this approach is that we had to take the complete annealing time for Δt, whereas it may have been shorter.

A macroscopic rheological measurement gives a different approach to flow properties and viscosity. In Figure 10, we have plotted the stress relaxation after an elongation to λ = 1.35 at 100 °C of a silica-free sample at pH 9. The sum of two single exponentials plus a constant level (about 10% of the total amplitude) allows describing the relaxation. One can extract from such a fit three different time scales: a short one (τ_1 = 9 s), an intermediate one (τ_2 = 180 s), and finally a constant level. The latter may indicate that the system tends to slightly cross-link after strong annealing, or residual strong interactions between H beads, possibly favored by their acrylic acid layer. It may be noted that the observable time scales are much shorter than the annealing times. The mechanisms of stress relaxations leading to these time scales are unknown, and we conjecture that τ_1 is related to the chain motion and τ_2 associated with zone rearrangements. The intermediate relaxation time can then be related to η via the Maxwell relationship $\eta = G\tau_2 = E/3\tau_2$, where G is the shear modulus and E Young's modulus at the same temperature, and we find $\eta = 27 \times 10^6$ Pa s. The rheologically observed viscosity is thus of the same order of magnitude as the one extracted from the demixing kinetics as observed by SANS. Naturally, a lucky coincidence cannot be excluded, and one must also keep in mind the shortcomings mentioned above. More sophisticated models may lead to different numerical results. The mechanism of bead diffusion itself, e.g., may be more complicated and coupled to chain interdiffusion. In our simple model, such effects have been absorbed in a single quantity, the self-diffusion coefficient of beads. The agreement in magnitude may still be seen as an encouraging result.

In the light of the experimental findings of this section, it appears that the polymer bead demixing kinetics as seen by SANS can be used as an indicator for the polymer dynamics. In the presence of 15 vol % of silica, dispersed in aggregates of small aggregation number (pH 9), the polymer bead dynamics is considerably slowed down as compared to the silica-free samples. Among the different scenarios previously discussed, the glassy layer hypothesis offers a plausible explanation. The estimated thickness of this layer is nanometric at temperatures not too far above the bulk glass-transition temperature; i.e., it is roughly of the same magnitude as the silica radius, doubling the radius of hard matter. A simple estimation of the total amount of frozen sample for our silica particles assuming individual dispersion and nonoverlapping frozen layers thus leads to an increase by a factor of $\approx 2^3$, which—starting from 15 vol %—means that the entire sample volume is frozen at temperatures close to the bulk T_g.

This agrees with our observations of a blocked radius for H and D zones in the presence of 15 vol % of silica. It gives also an explanation for the strong reinforcement and maximum rupture energy observed at 15%, where energy dissipation by breakup of both aggregates and glassy zones may contribute. On the other hand, it implies that longer annealing procedures at higher temperatures are needed to observe the kinetics in this case.

VI. CONCLUDING REMARKS

The dispersion of silica nanoparticles in a matrix made of nanolatex has been characterized by TEM and SANS and summarized in the form of an aggregation diagram. Within this diagram, we have shown that it is possible to identify paths in parameters (concentration, pH) where the average aggregation number remains constant. This opens the possibility to check the impact of nanoparticle aggregate size on the reinforcement effect of model nanocomposites. Our results show that within

experimentally accessible bounds (N_{agg} = tens to one hundred) the effect of aggregate size on the low deformation reinforcement is too weak to be detected. If there is an effect of aggregate mass in this range, it is of limited impact, and may possibly be counterbalanced by small changes in compacity. In contrast, the influence of filler volume fraction is dominant and suggests the formation of a network of aggregates around Φ_{si} = 15%. This is found to affect the high-deformation behavior expressed in terms of the rupture energy, which presents a maximum for all pH values at Φ_{si} = 15%. We think that the similar compacity of aggregates (κ = 10−20%) makes them reach percolation at approximately the same volume fraction. The reinforcement is thus dominated by the silica aggregate volume fraction, but it can be modulated by additional phenomena, like the existence of sticky interactions between filler and polymer, or glassy zones. The polymer dynamics was thus studied in a second series of experiments. Deuterated polymer beads were introduced in latex form in the nanocomposites, and their demixing kinetics was studied, in the absence and presence of silica. It was found that silica hinders the bead motion, whereas in the absence of nanoparticles the domains grow, in agreement with a rudimentary model based on the local polymer viscosity. The observed polymer immobility in presence of filler affects the reinforcement by moving the system closer to mechanical percolation. Because of comparable compacities, the proximity to percolation is expected to be similar in all samples.

To conclude, three interesting perspectives of the present work may be mentioned. First, a simplified analysis allowed us to account for the (robust) experimental observations of domain growth. However, more elaborate theoretical modeling of all results will be necessary. Second, it would be interesting to control the aggregation numbers over a larger range, by modifying possibly both the ionic equilibria which determine the interparticle potentials in solution, and the kinetics of film formation. Finally, synthesis of latex particles forming compatible matrices might allow the observation of the mixing kinetics, up to molecular dispersion.[76] Incidentally, this should allow the measurement of chain conformation, which is one of the topics currently of interest in the field.

■ ASSOCIATED CONTENT

Ⓢ Supporting Information. Figures 1−8. This material is available free of charge via the Internet at http://pubs.acs.org.

■ AUTHOR INFORMATION

Corresponding Author
*E-mail: Anne-Caroline.Genix@univ-montp2.fr.

■ ACKNOWLEDGMENT

Stock solutions of silica and hydrogenated latex nanoparticles were gifts from Akzo Nobel and Rhodia, respectively. Pascal Martinez, Jean-Marc Fromental, and Sébastien Clément (all L2C) are thanked for their contributions to the construction of the strain rig. This work was conducted within the scientific program of the European Network of Excellence *Softcomp*: "Soft Matter Composites: an approach to nanoscale functional materials", supported by the European Commission. Financial support by a "chercheur d'avenir" grant (J.O.) of the Languedoc-Roussillon region is gratefully acknowledged. M.T. thanks ILL for financing her PhD within the ILL international PhD program.

■ REFERENCES

(1) Klüppel, M. *Adv. Polym. Sci.* **2003**, *164*, 1–86.
(2) Heinrich, G.; Kluppel, M.; Vilgis, T. A. *Curr. Opin. Solid State Mater. Sci.* **2002**, *6* (3), 195–203.
(3) Mark, J. E.; Erman, B.; Eirich, F. R. *Science and Technology of Rubber*; Academic Press: San Diego, 1994.
(4) Schmidt, G.; Malwitz, M. M. *Curr. Opin. Colloid Interface Sci.* **2003**, *8* (1), 103–108.
(5) Kohls, D. J.; Beaucage, G. *Curr. Opin. Solid State Mater. Sci.* **2002**, *6* (3), 183–194.
(6) El Harrak, A.; Carrot, G.; Oberdisse, J.; Eychenne-Baron, C.; Boue, F. *Macromolecules* **2004**, *37* (17), 6376–6384.
(7) El Harrak, A.; Carrot, G.; Oberdisse, J.; Jestin, J.; Boue, F. *Macromol. Symp.* **2005**, *226*, 263–278.
(8) El Harrak, A.; Carrot, G.; Oberdisse, J.; Jestin, J.; Boue, F. *Polymer* **2005**, *46* (4), 1095–1104.
(9) Chevigny, C.; Dalmas, F.; Di Cola, E.; Gigmes, D.; Bertin, D.; Boué, F.; Jestin, J. *Macromolecules* **2011**, *44* (1), 122.
(10) Inoubli, R.; Dagreou, S.; Lapp, A.; Billon, L.; Peyrelasse, J. *Langmuir* **2006**, *22* (15), 6683–6689.
(11) Berriot, J.; Montes, H.; Martin, F.; Mauger, M.; Pyckhout-Hintzen, W.; Meier, G.; Frielinghaus, H. *Polymer* **2003**, *44* (17), 4909–4919.
(12) Mark, J. E.; Jiang, C. Y.; Tang, M. Y. *Macromolecules* **1984**, *17* (12), 2613–2616.
(13) Choi, S. S. *J. Polym. Sci., Part B: Polym. Phys.* **2001**, *39* (4), 439–445.
(14) Jouault, N.; Dalmas, F.; Said, S.; Di Cola, E.; Schweins, R.; Jestin, J.; Boué, F. *Phys. Rev. E* **2010**, *82* (3), 031801.
(15) Jouault, N.; Dalmas, F.; Said, S.; Di Cola, E.; Schweins, R.; Jestin, J.; Boué, F. *Macromolecules* **2010**, *43* (23), 9881.
(16) Boisvert, J. P.; Persello, J.; Guyard, A. *J. Polym. Sci., Part B: Polym. Phys.* **2003**, *41* (23), 3127–3138.
(17) Guyard, A.; Persello, J.; Boisvert, J. P.; Cabane, B. *J. Polym. Sci., Part B: Polym. Phys.* **2006**, *44* (7), 1134–1146.
(18) Persello, J.; Boisvert, J. P.; Guyard, A.; Cabane, B. *J. Phys. Chem. B* **2004**, *108* (28), 9678–9684.
(19) Tuteja, A.; Duxbury, P. M.; Mackay, M. E. *Macromolecules* **2007**, *40* (26), 9427–9434.
(20) Chevalier, Y.; Hidalgo, M.; Cavaille, J. Y.; Cabane, B. *Abstr. Pap. Am. Chem. Soc.* **1995**, *210*, 50-Pmse.
(21) Chevalier, Y.; Pichot, C.; Graillat, C.; Joanicot, M.; Wong, K.; Maquet, J.; Lindner, P.; Cabane, B. *Colloid Polym. Sci.* **1992**, *270* (8), 806–821.
(22) Dingenouts, N.; Ballauff, M. *Kautschuk Gummi Kunststoffe* **1999**, *52* (10), 652–655.
(23) Dingenouts, N.; Ballauff, M. *Langmuir* **1999**, *15* (9), 3283–3288.
(24) Grillet, A. C.; Brunel, S.; Chevalier, Y.; Usoni, S.; Ansanay-Alex, V.; Allemand, J. *Polym. Int.* **2004**, *53* (5), 569–575.
(25) Joanicot, M.; Wong, K.; Cabane, B. *Macromolecules* **1996**, *29* (14), 4976–4984.
(26) Winnik, M. A. *Curr. Opin. Colloid Interface Sci.* **1997**, *2* (2), 192–199.
(27) Rharbi, Y.; Cabane, B.; Vacher, A.; Joanicot, M.; Boue, F. *Europhys. Lett.* **1999**, *46* (4), 472–478.
(28) Chevalier, Y.; Hidalgo, M.; Cavaille, J. Y.; Cabane, B. *Macromolecules* **1999**, *32* (23), 7887–7896.
(29) Chevalier, Y.; Hidalgo, M.; Cavaille, J. Y.; Cabane, B. *Prog. Org. Coat.* **1997**, *32* (1−4), 35–41.
(30) Oberdisse, J.; Deme, B. *Macromolecules* **2002**, *35* (11), 4397–4405.
(31) Oberdisse, J. *Macromolecules* **2002**, *35* (25), 9441–9450.
(32) Oberdisse, J.; Pyckhout-Hintzen, W.; Straube, E. Structure Determination of Polymer Nanocomposites by Small Angle Scattering. In *Recent Advances in Polymer Nanocomposites*; Thomas, S., Zaikov, G., Valsaraj, S. V., Eds.; Brill NV: Leiden, The Netherlands, 2009; p 397.

(33) Oberdisse, J. *Soft Matter* **2006**, *2* (1), 29–36.
(34) Oberdisse, J.; Hine, P.; Pyckhout-Hintzen, W. *Soft Matter* **2007**, *2*, 476–485.
(35) Rharbi, Y.; Boue, F.; Joanicot, M.; Cabane, B. *Macromolecules* **1996**, *29* (12), 4346–4359.
(36) Zhang, J. Q.; Hu, S. S.; Rieger, J.; Roth, S. V.; Gehrke, R.; Men, Y. F. *Macromolecules* **2008**, *41* (12), 4353–4357.
(37) Hu, S. S.; Rieger, J.; Lai, Y. Q.; Roth, S. V.; Gehrke, R.; Men, Y. F. *Macromolecules* **2008**, *41* (13), 5073–5076.
(38) Bolze, J.; Ballauff, M.; Kijlstra, J.; Rudhardt, D. *Macromol. Mater. Eng.* **2003**, *288* (6), 495–502.
(39) Einstein, A. *Ann. Phys.* **1906**, *19*, 289.
(40) Smallwood, H. M. *J. Appl. Phys.* **1944**, *15*, 758–766.
(41) Chabert, E.; Bornert, M.; Bourgeat-Lami, E.; Cavaillé, J.; Dendievel, R.; Gauthier, C.; Putaux, J.; Zaoui, A. *Mater. Sci. Eng., A* **2004**, *381*, 320.
(42) Long, D.; Lequeux, F. *Eur. Phys. J. E* **2001**, *4* (3), 371–387.
(43) Papon, A.; Saalwächter, K.; Schäler, K.; Guy, L.; Lequeux, F.; Montes, H. *Macromolecules* **2011**, *44*, 913–922.
(44) Kobayashi, M.; Rharbi, Y.; Brauge, L.; Cao, L.; Winnik, M. A. *Macromolecules* **2002**, *35*, 7387–7399.
(45) Triolo, A.; Celso, F. L.; Negroni, F.; Arrighi, V.; Qian, H.; Lechner, R. E.; Desmedt, A.; Pieper, J.; Frick, B.; Triolo, R. *Appl. Phys. A: Mater. Sci. Process.* **2002**, *74* (Suppl.), S490–S492.
(46) Arrighi, V.; Higgins, J. S.; Burgess, A. H.; Floudas, G. *Polymer* **1998**, *39* (25), 6369–6376.
(47) Anastasiadis, S. H.; Chrissopoulou, K.; Frick, B. *Mater. Sci. Eng., B* **2008**, *152* (1−3), 33–39.
(48) Berriot, J.; Lequeux, F.; Monnerie, L.; Montes, H.; Long, D.; Sotta, P. *J. Non-Cryst. Solids* **2002**, *307*, 719–724.
(49) Berriot, J.; Martin, F.; Montes, H.; Monnerie, L.; Sotta, P. *Polymer* **2003**, *44* (5), 1437–1447.
(50) Berriot, J.; Montes, H.; Lequeux, F.; Long, D.; Sotta, P. *Europhys. Lett.* **2003**, *64* (1), 50–56.
(51) Berriot, J.; Montes, H.; Lequeux, F.; Long, D.; Sotta, P. *Macromolecules* **2002**, *35* (26), 9756–9762.
(52) Montes, H.; Lequeux, F.; Berriot, J. *Macromolecules* **2003**, *36* (21), 8107–8118.
(53) Montes, H.; Chaussee, T.; Papon, A.; Lequeux, F.; Guy, L. *Eur. Phys. J. E* **2010**, *31* (3), 263–268.
(54) Summerfield, G. C.; Ullman, R. *Macromolecules* **1987**, *20*, 401–404.
(55) Yousfi, M.; Porcar, L.; Lindner, P.; Boué, F.; Rharbi, Y. *Macromolecules* **2009**, *42*, 2190–2197.
(56) Kim, S. D.; Klein, A.; Sperling, L. H.; Boczar, E. M.; Bauer, B. J. *Macromolecules* **2000**, *33*, 8334–8343.
(57) Kim, K. D.; Sperling, L. H.; Klein, A.; Wignall, G. D. *Macromolecules* **1993**, *26*, 4624–4631.
(58) Still, T.; Retsch, M.; Jonas, U.; Sainidou, R.; Rembert, P.; Mpoukouvalas, K.; Fytas, G. *Macromolecules* **2010**, *43* (7), 3422–3428.
(59) Mark, J. E. *Physical Properties of Polymers Handbook*; AIP Press: Woodbury, NY, 1996.
(60) Unzueta, E.; Forcada, J. *Polymer* **1995**, *36* (22), 4301–4308.
(61) Lindner, P. *Neutrons, X-ray and Light Scattering*; Elsevier: Amsterdam, 2002.
(62) Oberdisse, J.; Rharbi, Y.; Boue, F. *Comput. Theor. Polym. Sci.* **2000**, *10* (1−2), 207–217.
(63) Schaefer, D. W.; Rieker, T.; Agamalian, M.; Lin, J. S.; Fischer, D.; Sukumaran, S.; Chen, C. Y.; Beaucage, G.; Herd, C.; Ivie, J. *J. Appl. Crystallogr.* **2000**, *33* (1), 587–591.
(64) Beaucage, G. *Phys. Rev. E* **2004**, *70* (3), xxxx.
(65) Beaucage, G. *J. Appl. Crystallogr.* **1995**, *28*, 717–728.
(66) Witten, T. A.; Rubinstein, M.; Colby, R. H. *J. Phys. II* **1993**, *3* (3), 367–383.
(67) Ahmed, S.; Jones, F. R. *J. Mater. Sci.* **1990**, *25* (12), 4933–4942.
(68) Guth, E. *J. Appl. Phys.* **1945**, *16*, 20–25.
(69) Guth, E.; Gold, O. *Phys. Rev.* **1938**, *53*, 322.
(70) Mooney, M. *J. Colloid Sci.* **1951**, *6*, 162.
(71) Jouault, N.; Vallat, P.; Dalmas, F.; Said, S.; Jestin, J.; Boue, F. *Macromolecules* **2009**, *42* (6), 2031–2040.
(72) Nakatani, A.; Chen, W.; Schmidt, R.; Gordon, G.; Han, C. *Polymer* **2001**, *42*, 3713–3722.
(73) Nusser, K.; Neueder, S.; Schneider, G. J.; Meyer, M.; Pyckhout-Hintzen, W.; Willner, L.; Radulescu, A.; Richter, D. *Macromolecules* **2010**, *43* (23), 9837–9847.
(74) Sen, S.; Xie, Y.; Kumar, S. K.; Yang, H.; Bansal, A.; Ho, D. L.; Hall, L.; Hooper, J. B.; Schweizer, K. S. *Phys. Rev. Lett.* **2007**, *98*, 128302.
(75) Tuteja, A.; Duxbury, P.; Mackay, M. *Phys. Rev. Lett.* **2008**, *100*, 077801.
(76) Tatou, M. Manuscript in preparation.
(77) Tatou, M. Nanocomposites modèles silice-latex: Etude des propriétés rhéologiques et de la structure des charges et des chaînes par Diffusion de Neutrons aux Petits Angles, University of Montpellier II, Montpellier, 2010.
(78) Cotton, J. P.; Decker, D.; Benoit, H.; Farnoux, B.; Higgins, J.; Jannink, G.; Ober, R.; Picot, C.; Cloizeau, J. D. *Macromolecules* **1974**, *7* (6), 863–872.
(79) Cotton, J. P. *Adv. Colloid Interface Sci.* **1996**, *69*, 1–29.
(80) Cotton, J. P.; Hardouin, F. *Prog. Polym. Sci.* **1997**, *22* (4), 795–828.
(81) Benoit, H. C.; Higgins, J. S. *Polymers and Neutron Scattering*; Oxford University Press: Oxford, 1994.
(82) de Gennes, P.-G. *Scaling Concepts in Polymer Physics*; Cornell University Press: Ithaca, NY, 1979.
(83) Bates, F. S.; Fetters, L. J.; Wignall, G. D. *Macromolecules* **1988**, *21* (4), 1086–1094.
(84) Paul, D. R.; Bucknall, C. B. *Polymer Blends*; Wiley-Interscience: New York, 2000.
(85) Gam, S.; Meth, J. S.; Zane, S. G.; Chi, C. Z.; Wood, B. A.; Seitz, M. E.; Winey, K. I.; Clarke, N.; Composto, R. J. *Macromolecules* **2011**, *44* (9), 3494–3501.